nature reviews physics

https://doi.org/10.1038/s42254-024-00764-7

Review article

Check for updates

Petahertz electronics

Christian Heide [1,2] ✉, Phillip D. Keathley [3] & Matthias F. Kling [1,2]

Abstract

Petahertz, or lightwave, electronics uses tailored optical waveforms to control charge carriers in an electronic circuit at petahertz frequencies. This may enable faster processing than conventional pulsed electronics, which cannot be scaled beyond gigahertz frequencies. In recent years, petahertz-scale currents driven by optical fields have been measured in solid-state systems and nanoscale structures, with several proof-of-principle demonstrations of sub-optical-cycle current generation and optical-field-resolved waveform detection at the sub-femtosecond to few-femtosecond scale. Recent work has taken the first steps towards digital and quantum operation by exploring optical-field-driven logic and memory functionality. In this Review, we discuss the progress towards sub-cycle field-driven current injection, highlighting key theoretical concepts, experimental milestones, and questions remaining as we push towards realizing petahertz electronics for ultrafast optical waveform analysis, digital logic, communications, and quantum computation.

Sections

[1]Department of Applied Physics, Stanford University, Stanford, CA, USA. [2]Stanford PULSE Institute, SLAC National Accelerator Laboratory, Menlo Park, CA, USA. [3]Research Laboratory of Electronics, Massachusetts Institute of Technology, Cambridge, MA, USA. ✉e-mail: cheide@stanford.edu

Introduction

Despite tremendous efforts of the semiconductor industry, the clock rate of today's electronics has levelled off to a few gigahertz. Although the frequency of electromagnetic fields can be continuously increased, a limit is reached at which the corresponding photon energy is sufficient to inject charge across energy barriers, and the field is no longer the primary driver of the current (Fig. 1). Possible solutions to achieve faster responses, such as petahertz-fast electronics, have been proposed, such as leveraging optical nonlinearities, nonlinear wave mixing and interactions with single-femtosecond laser pulses, but these methods are not easily scalable nor optimized for compact, on-chip applications. A more promising approach combines tailored optical light fields and alternative materials and systems that continue to behave electronically when driven at optical frequencies. That is, devices and systems where the emitted current has a non-perturbative electronic response, directly sensitive to the field of the driving light waveforms rather than their time-averaged intensity.

About 20 years ago, experiments using intense laser fields to control the flow of electrons were demonstrated in the gas phase, wherein the strong optical field tunnel ionizes an atom within a fraction of an optical cycle. These studies have heralded the birth of attosecond science[1–3] and enabled the microscopic control of electrons in vacuum with precision limited only by quantum mechanical uncertainty[4]. A decade later, petahertz-scale tunnel ionization and electron control was demonstrated from the surface of nanoparticles[5], nanoscale needle tips[6,7] and planarized nanostructures on chip surfaces[8–10]. The compactness of these systems combined with plasmonic and geometric field enhancement[11,12] has since relaxed the need for bulky, high-intensity laser setups, as used in early gas-phase experiments. Sub-cycle electron emission at hundreds of terahertz to petahertz has since been demonstrated in nanoantenna arrays, with optical fields driving the tunnelling emission of electrons[13–19].

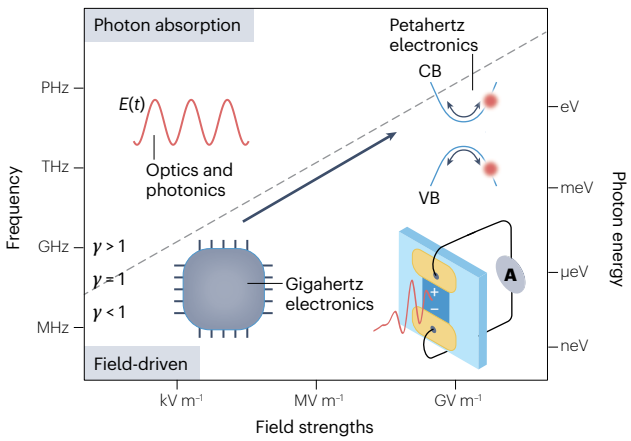

Fig. 1 | Electric-field versus photon-driven electronics. In gigahertz electronics (bottom left), electric fields with a strength of around E_0 ~ 0.1 kV m^{-1} control the current flow, allowing for switching, rectification and, ultimately, computing. In optics, electromagnetic fields oscillating at 100 THz to petahertz frequencies can be generated using laser sources (top left). However, with increasing frequency, a limit is reached wherein the charge generation mechanism inside of solids is slow compared to the cycle duration of the driving field, and cycle-averaged photon-based absorption governs the device response. To increase the speed of the current generation mechanism to petahertz-scale frequencies, an electric field strength of E_0 ~ GV m^{-1} is required (top right). These fields can be achieved with tailored ultrashort laser pulses. The grey-dashed line represents the condition wherein the driving frequency equals the frequency of current injection in GaAs. Below this line, the current generation mechanism is sensitive to the electric field waveform, allowing for lightwave or petahertz electronics, whereas above the line, the response is governed by photon absorption. The scale on the right indicates the associated photon energy. CB, conduction band; VB, valence band.

Building on the success of attosecond-fast control of electron emission in the gas phase and in nanostructures, on-chip integration and increased efficiency may benefit from the control of currents directly inside of the solids and their device structures. Although electron control inside solids was initially considered unsuitable for petahertz-fast current control, mainly owing to degradation, fast scattering and dephasing, with the observation of non-perturbative high-harmonic generation and sub-femtosecond solid-state spectroscopy, it turned out that light-field-driven electron dynamics inside solids at petahertz frequencies is possible, in particular, when driven off-resonantly and with ultrashort laser pulses[20–28]. Since its demonstration in fused silica[23] a decade ago, various compact, chip-scale elements have demonstrated the control of charge carriers at petahertz frequencies and the creation of sub-femtosecond current bursts in a range of materials and systems, including the semimetal graphene[27,29–32], semiconductors[33–35] and dielectrics[23,35–37].

In analogy with terahertz and gigahertz electronics, these solid-state platforms that enable sub-cycle, optical-field-driven control of current injection have been coined petahertz electronics[13,14,38,39]. Compared to the first experiments in dielectrics, the required peak energy has been reduced by ten orders of magnitude through the application of novel materials and miniaturization, nanoplasmonics, pump-probe schemes and the development of powerful waveform-controlled high repetition-rate light sources in the near-infrared and mid-infrared spectral range, making this technology accessible to many laboratories and applications.

In the past 5 years, a logic gate[40], light-field current switching[23,41], random-access memory[42], spintronics and valleytronics[43–47], topotronics[48], with all-optical anomalous Hall photocurrents, valley currents and photocurrent circular dichroism, Bloch electron wave control and splitting at ambient temperature[27,32], and data encoding[49,50] have been predicted and demonstrated at terahertz to petahertz frequencies. In addition, petahertz-scale light-field sampling has been pioneered[15,23,51–54], analogous to a sampling oscilloscope for optical field waveforms, providing critical tools for fundamental science and the further analysis and development of petahertz electronics. Furthermore, petahertz electronics has clear ramifications for material spectroscopy, as it provides direct access to novel solid-state properties, such as quantum-mechanical phases[22,32], topological properties[55–58], strong electron correlations[59–61], and ultrafast magnetism[62], offering a new paradigm for future lightwave spectroscopy and electronics[63].

In this Review, we provide an overview of sub-optical-cycle, electric-field-driven current responses in bulk media, at interfaces and at nanostructured systems. Next, we focus on applications that have ushered in the analog age of petahertz electronics, in particular carrier-envelope phase (CEP) detection and sub-cycle optical field sampling. Finally, we review theoretical proposals for transitioning from analog petahertz electronics to integrated classical and quantum-based petahertz logic operations and provide an outlook towards future research directions.

Sub-cycle electric field response

We start our discussion by providing an overview on how a lightwave interacts with electrons in a solid and how this can be used to build

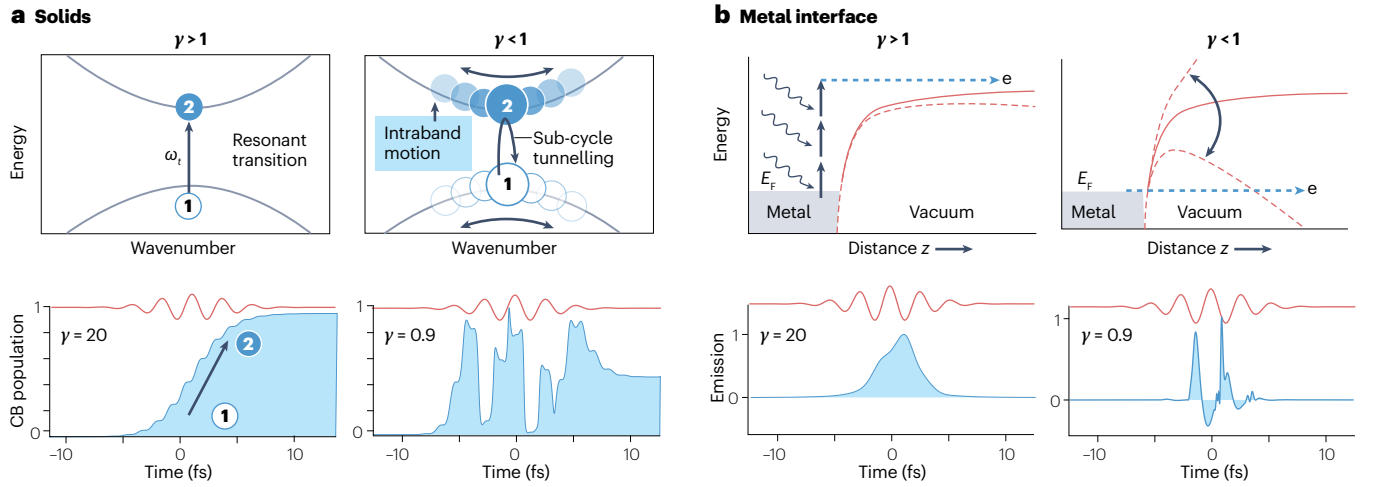

Fig. 2 | Electron dynamics in condensed media and at metal interfaces. **a**, The electron dynamics in the conduction band and valence band (top) and associated time-resolved population dynamics (bottom) within a solid after interaction with a laser pulse. For a laser pulse with a low intensity, that is, $\gamma = 20$, the population builds up gradually during the laser pulse and can be described via photon-based absorption. The additional oscillation, which is twice the frequency of the laser, is known as Bloch–Siegert oscillation. For an intense laser pulse, that is, $\gamma = 0.9$, the electron dynamics is faster than an optical cycle of the driving pulse and the band population strongly depends on the shape of the electric field waveform. **b**, Light-induced tunnel ionization from a metal–vacuum interface (top) and corresponding temporal emission (bottom). Similarly, for $\gamma = 20$, the electron emission is mostly following the pulse envelop, whereas for $\gamma = 0.9$, the electron wavefunction is driven from the metal to vacuum on a sub-cycle timescale of the lase field.

petahertz electronics. When a lightwave interacts with electrons in the band structure, the optical field of light $E(t)$ transiently accelerates Bloch electrons by imparting a time-dependent momentum $\dot{k}(t)$ to the electrons. The amount of momentum transferred is described by Bloch's acceleration theorem[64]

$$\dot{k}(t) = e\hbar^{-1} E(t), \quad (1)$$

with e the elementary charge and $\hbar$ the reduced Planck constant. Although equation (1) generates an oscillating dipole, it does not mean that a measurable current sensitive to the exact shape of $E(t)$ emerges. To obtain a residual current sensitive to the shape of $E(t)$, which can be measured within a circuit, the current needs to be injected within a timescale below the cycle duration of the driving optical waveform. As we will discuss later, this can be achieved via sub-cycle quantum path interference in bulk materials or sub-cycle charge transfer and induction at interfaces.

In the context of the current generation within a solid, the crucial parameter describing the speed of the current generation is the time it takes for an electron to undergo a band-to-band transition[65–67]. Similarly, at a material interface, such as a metal–vacuum or material–material transition, it is the tunnelling time that sets the speed limit and its associated frequency, defined as angular tunnel frequency ω_t (Fig. 2). The comparison of this transition time to the angular driving frequency of the laser ω defines the light-field-driven regime, categorized by the Keldysh adiabaticity parameter $\gamma = \omega/\omega_t$ (refs. 65,67,68). If $\gamma < 1$, the electron transition from one band to the other, or from the metal to vacuum occurs on a sub-cycle timescale and, thus, the excitation or ionization and, ultimately, the measured current may be sensitive to $E(t)$. For $\gamma > 1$, the transition time is too slow to generate a residual current sensitive to the electric field waveform, and the electron dynamics follow the time-averaged intensity of the excitation pulse (its pulse envelope) and, thus, is not directly sensitive to the shape of the applied waveform.

Calculating tunnelling frequencies

For a band-to-band transition in bulk media (Fig. 2a), the tunnelling frequency can be estimated as $\omega_t = \frac{eE_0}{\sqrt{m_{e,\mathrm{eff}}\Delta}}$, with E_0 being the applied optical field strengths. For example, to obtain $\gamma < 1$ in GaAs, a semiconductor relevant in electronics (with an effective electron mass: $m_{e,\mathrm{eff}} = 0.067\, m_e$, bandgap: $\Delta = 1.42$ eV) at 0.375 PHz (wavelength of 800 nm), a minimal electric field strength of $E_0 > 1.7$ V nm^{-1} is required. The bottom panels in Fig. 2a show the conduction band population as a function of time for two different field strengths and, thus, two different values of γ. For $\gamma > 1$ (left), the emission gradually builds up during the laser pulse, whereas for $\gamma < 1$ (right), the population dynamics are sensitive to the electric field waveform.

In the case of tunnel ionization from metal to vacuum, the tunnel frequency can be estimated as $\omega_t = \frac{eE_0}{\sqrt{2m_e\Phi}}$, with Φ being the work function of the metal, which is $\Phi = 5$ eV for typical metals. To estimate the field required to achieve a sub-cycle response such that $\gamma < 1$, at 0.375 PHz, a field strength of $E_0 > 18$ V nm^{-1} is required to drive sub-cycle tunnel ionization. The bottom panels of Fig. 2b show the current emission as a function of time for two different field strengths and, thus, two different values of γ. For $\gamma > 1$ (left), the emission mostly follows the intensity envelope of the laser pulse, whereas for $\gamma < 1$ (right), the emission dynamics are sensitive to the electric field waveform.

On the basis of these estimates, we can see that building petahertz electronics using semiconductors with a bandgap of ~eV requires an electric field strength on the order of ~V nm^{-1}. In the case of sub-cycle tunnel ionization from a metal surface, the required electric field strength is about ten times higher than for the sub-cycle band-to-band transition in semiconductors, which can be understood based on the reduced energy gap to transition from the valence to the conduction band, compared to the ionization potential in metals, and secondly, the effective electron mass is reduced in semiconductors, compared to free space ($m_{e,\mathrm{eff}} < m_e$).

To speed up the transition frequency and ultimately obtain a system response sensitive to $E(t)$, the electric field amplitude that drives

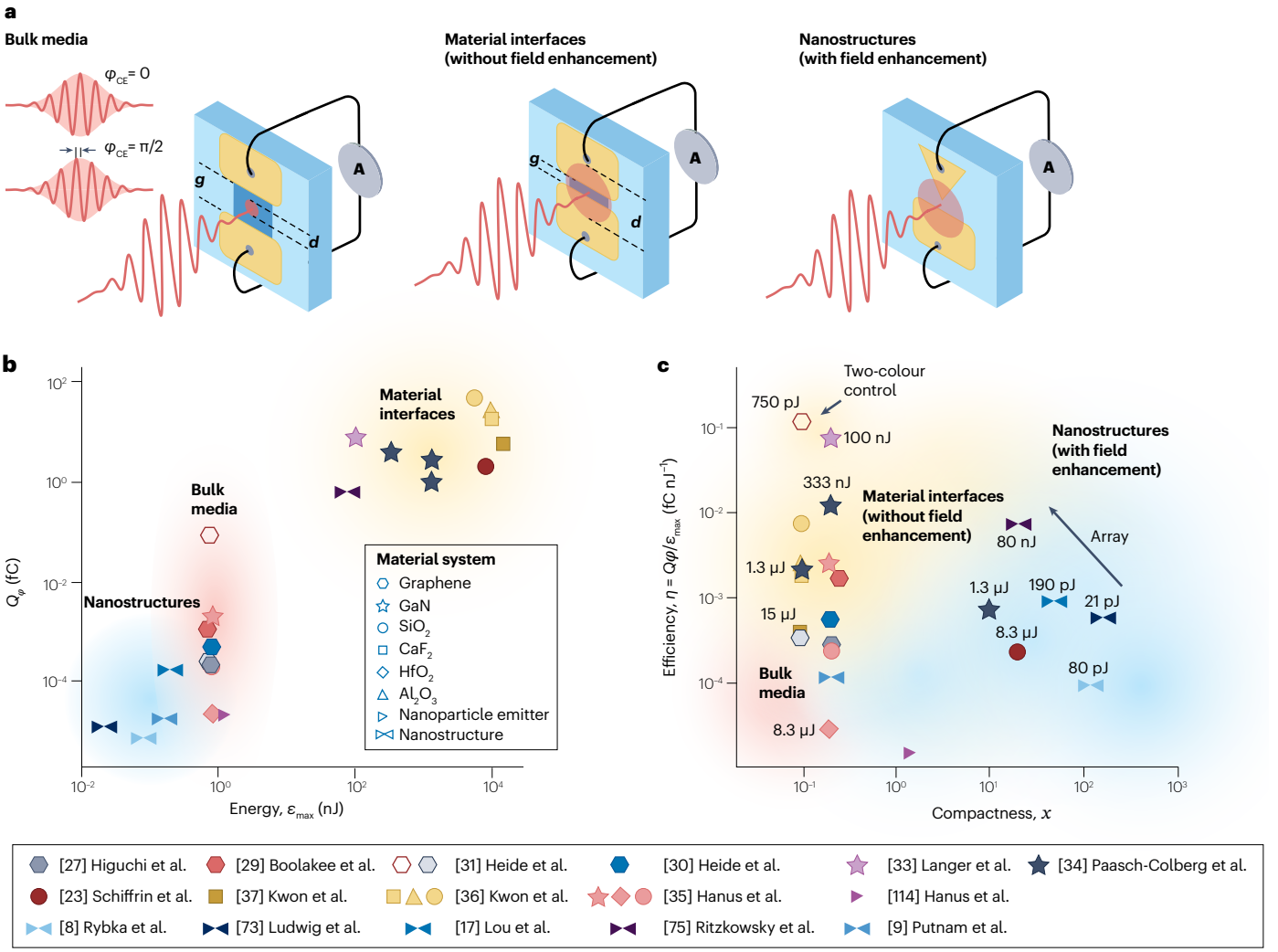

Fig. 3 | Recent progress in petahertz current injection. a, Device schemes for current injection in bulk media (spot size d smaller than electrode gap g) at material interfaces ($d > g$) and within nanostructured systems providing field enhancement. **b**, Maximal carrier-envelope phase-sensitive charge injection Q_φ plotted as a function of pulse energy for various material systems including semimetals (graphene[27,29–31]), semiconductors (GaN (refs. 33–35)), dielectrics (SiO_2 (refs. 23,35,36), CaF_2 (refs. 36,37), HfO_2 (ref. 35) and Al_2O_3 (ref. 36)), and nanostructures[8,9,14]. The three device schemes are highlighted in red (bulk), yellow (material interfaces, without field enhancement) and blue (nanostructured systems designed for field enhancement). **c**, To compare various experimental conditions, we plot the efficiency η, defined as the ratio of Q_φ and pulse energy ε_{max}, versus the compactness χ of the device (inverse electrode separation g). More relevant experimental parameters and a performance comparison can be found in the Supplementary information.

the current needs to be increased, also illustrated as field-driven regime in Fig. 1. One possibility to increase the peak electric field strengths of the laser pulse without damaging the material is to use off-resonant excitation and to decrease the pulse duration while maintaining the pulse energy. With a combination of tight focusing, a resonant electromagnetic response (for example, plasmonics) and nanostructured features for geometric field enhancement, it is possible to obtain field strengths in the order of ~V nm^{-1} from picojoule laser pulses at a repetition rate of tens of megahertz. Furthermore, with frequency combs[69], it is now possible to stabilize and synthesize optical lightwaves, similar to what was done for radiowaves, which was an essential breakthrough in precisely controlling electrons in free space or solids[4,8,9,13,14,27,30,31,33–36,40,69–72].

Systems and materials for petahertz electronics

Petahertz-fast current generation has been experimentally demonstrated in numerous materials and systems, such as in the semimetal graphene[27,29–31], semiconductors[33–35], dielectrics[23,35–37], and on-chip nanostructures and nanostructure arrays[8,9,14,15,17,73,74]. To inject petahertz-scale current in bulk media, material interfaces and nanostructures, phase-stabilized few-cycle laser pulses are applied (Fig. 3a). The field oscillations' timing to the pulse peak is determined by CEP φ_{CE}. For few-cycle laser pulses, a change in φ_{CE} substantially changes the temporal evolution of the field waveform. This is shown for a few-cycle long cosine or sine-like waveform in Fig. 3a. Thus, by changing φ_{CE}, the degree of time asymmetry of the laser pulse can be controlled, which may result in a non-zero residual waveform-sensitive current. Note that

this asymmetry can be increased with two-colour[31] or near-single-cycle pulses, which may result in a larger waveform-sensitive currents.

Given that CEP-sensitive current, together with a non-perturbative response, is a good indicator of waveform-sensitive current, it can be used as a metric for comparing the performance of various types of petahertz electronic devices. In Fig. 3b we plot the CEP-sensitive charge Q_φ versus the applied pulse energy ε_{max} for a variety of petahertz-electronic devices. Furthermore, we plot the efficiency, $\eta = Q_\varphi/\varepsilon_{max}$ versus the compactness of the device (inverse electrode distance) in Fig. 3c. Compactness might become relevant in future miniaturized devices, wherein many components must be positioned in a finite area (or volume). Before we discuss the underlying current generation mechanisms for each case in the subsequent sections, we first briefly compare the efficiency and performance of these systems.

In general, bulk media offer a large photoactive area[27,29–31,35], potentially yielding many waveform-dependent photocarriers, but injected carriers with a net momentum may recombine before reaching the electrodes, reducing efficiency. Additionally, materials with small bandgaps generate a large number of resonant photocarriers which are unwanted as they are often waveform-independent while also increasing both decoherence and heat load which can result in damage to the device structure. By contrast, direct illumination of interfaces between large bandgap materials (such as SiO_2 or GaN) and metals can provide dominantly sub-cycle, waveform-dependent current injection. However, the increased bandgap necessitates high electric fields, and thus increased pulse energy, for efficient tunnelling over the energy barrier (in this case, tunnelling through Schottky junction or ionization)[23,33,34,36,37]. Nanostructures provide field enhancement, reducing the needed incident field strength (and thus pulse energy), but at the cost of reduced waveform-sensitive current due to the reduced dimensionality[8,14,73]. To overcome this reduced efficiency in generating waveform-sensitive current the nanostructures can be arranged in arrays, greatly increasing the active area of the device[75]. Furthermore, enhancing CEP-dependent current could be achieved through local field enhancement in bulk media[76], multilayered materials[77], patterned electrodes, or layered and denser nanostructure arrays.

Bulk media

For the case of bulk media, a CEP-stabilized laser field illuminates the solid and injects a residual waveform-sensitive current measured with two metal electrodes. We note that such measurements have been performed using photon-based ($\gamma > 1$) quantum-path interference (known as quantum control) for more than 30 years using two-colour or multi-colour optical fields[78–81], but currents generated in this way have not been on a sub-cycle timescale of the laser field; hence, this scheme is not well suited for petahertz electronics. Here, we focus on the strong-field counterpart with sub-cycle-controlled quantum-path interference and femtosecond-fast current injection, $\gamma < 1$.

With CEP-stable, few-cycle laser pulses, it has been demonstrated that intraband motion and interband transitions are coupled at large field strengths, and that electrons undergo Landau–Zener transitions between valence and conduction bands. Electrons can even undergo two subsequent Landau–Zener transitions when they are driven back and forth across the apparent bandgap minimum by the oscillating light field[27,30,41] (Fig. 4a,b). At a wavelength of 800 nm, these two transition events are only separated in time by half an optical cycle (~1.3 fs). At such short timescales, electronic matter wave coherence is fully preserved. Because the Landau–Zener transition events act as electron beam splitters, an electron interferometer akin to a Mach–Zehnder interferometer has been demonstrated. The quantum phase accumulated in the beam-split state determines whether the electron ends up in the valence or the conduction band. This type of interferometer is called a Landau–Zener–Stückelberg–Majorona (LZSM) interferometer[82–85]. Intriguingly, the interferometer action happens so fast that for an asymmetric vector potential, a current emerges within 1 fs.

Although LZSM interferometry can in principle be observed in various systems, graphene serves as an ideal model system for such measurements, as it has a high conductivity and a simple band structure, which can often be described with two electronic bands[86]. To experimentally demonstrate petahertz-fast current injection in graphene, few-cycle laser pulses are focused on the centre of a symmetric electrode–graphene–electrode device. By increasing E_0, the measured current scales non-monotonically, with several current reversals around 2 and 3 V nm^{-1}, indicating sub-cycle-controlled LZSM interferometry[30,32] (Fig. 4c). The observation of LZSM interferometry in graphene highlights a number of key points. The field of light is controlling electrons at optical frequencies, with petahertz-fast LZ transitions events. The electron dynamics during an optical cycle remains coherent, and based on a comparison with model simulations, the residual current peaks for $\varphi_{CE} = \pm\pi/2$, when the vector potential $A(t)$ breaks the inversion symmetry. Such a non-perturbative current increase has also been found in GaN, HfO_2 and SiO_2 (refs. 23,33–37) (Fig. 4d). However, a non-monotonic current response as a function of E_0 has not been observed, most probably because compared to graphene, the bandgap of these materials is larger, which may require a larger electric field strength or longer wavelengths to drive LZSM interferometry.

Modelling petahertz-fast ballistic current injection. The microscopic description of the generation of petahertz currents in solids is still in its infancy. Within the past 10 years, various theoretical models have been developed to describe the generation and detection mechanisms of the CEP-dependent petahertz current in solids. This includes the time-dependent Dirac equation[87,88], time-dependent Schrodinger equation[27,89,90], semiconductor Bloch equations[91], ab initio simulations[86,92] and real space simulations without[93] and with contact electrodes[40,94]. These simulations can capture the complex electric field dependence (Fig. 4c), the polarization dependence[41] and electronic dephasing[95]. However, reproducing the amplitude of the measured charge density is challenging as the charge propagation after injection and charge detection at the interfaces exceed current model simulations.

Recent theoretical studies and initial experimental demonstration highlight that quantum materials with long coherence times or high nonlinearities, such as transition metal dichalcogenide monolayers[90], organic superconductors[60], topologically protected materials[96], Weyl materials[97] or bilayer graphene[98,99], are promising candidates for future petahertz electronics. In particular, advanced electron control schemes become possible when combined with temporal pulse shaping[100–102] and polarization control[103]. This includes access to spin currents, valley currents and Hall currents[44–48,104–106]. Furthermore, vectorized electronics[107] and structured light[108] provide additional tools for generating arbitrary superpositions of orthogonal current modes, demonstrating the potential for reconfigurable 'virtual' petahertz electronic circuits[109,110].

Lightwave band engineering and valley control. Whereas petahertz electronics aims to control charge carrier dynamics in materials at

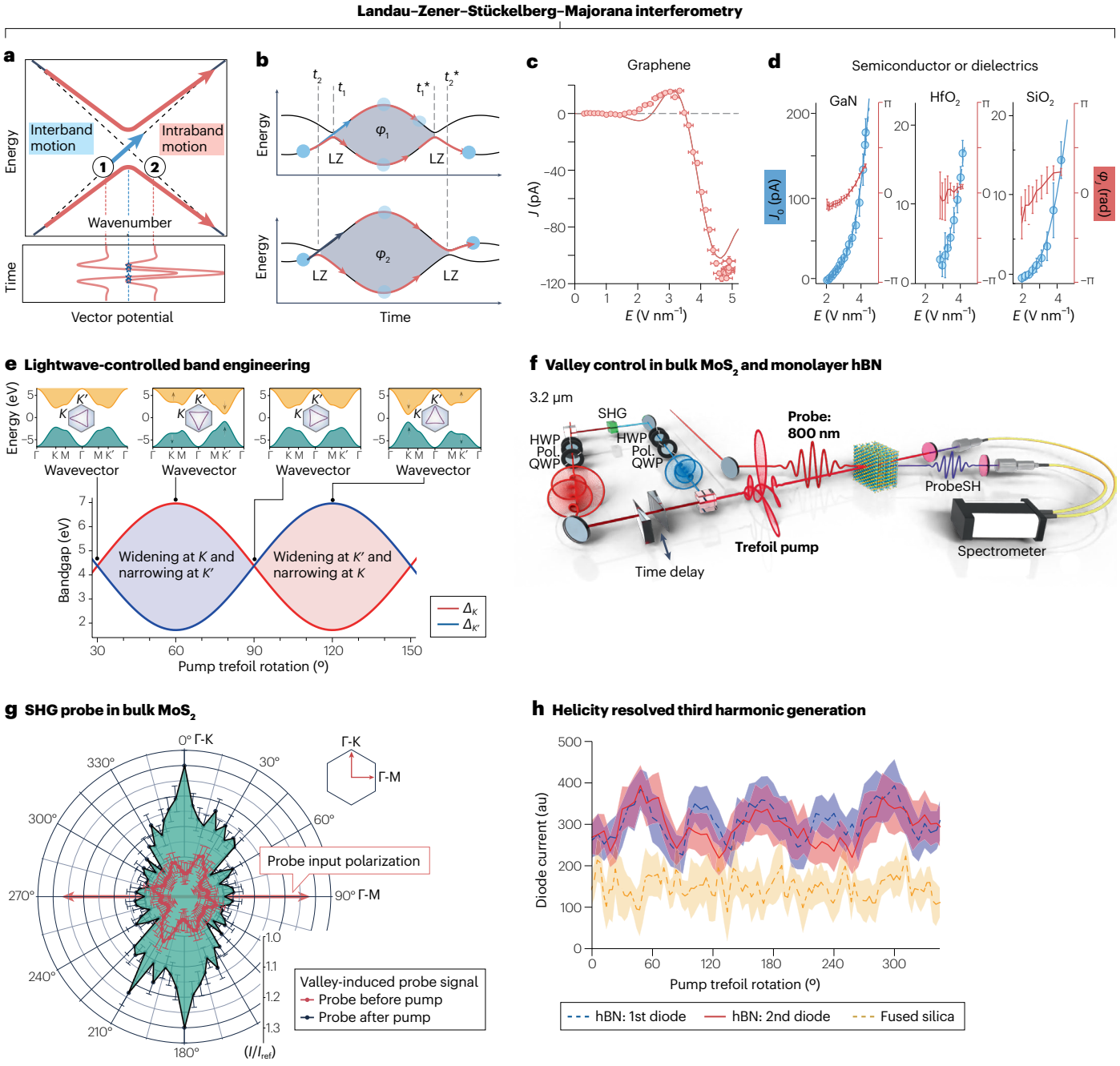

sub-cycle speeds of the lightwave, further concepts to encode and store information as classical or quantum bits are needed to boost lightwave-based information processing. The recently demonstrated sub-cycle-controlled, non-resonant valleytronics is an interesting prospect in this direction[46–48]. Here, purpose-tailored and intense lightwaves on the order of ~V nm^{-1} are applied to solids to control the spatial-inversion and time-reversal symmetries, which allow control over magnitude, location and curvature of the bandgap, enabling ultrafast valley control and read out (Fig. 4e).

For example, in hexagonal materials, such as graphene, boron nitride (hBN) or bulk MoS_2 (refs. 46–48,104,111), a trefoil control electric field can induce complex second-neighbour hopping, lifting valley degeneracy. As the field and its associated vector potential rotate in space, the band structure is modified, causing the effective bandgap to oscillate with the rotation of the trefoil light field. This may lead to varying electron excitation dynamics between the valleys and a valley polarization. Using a pump-probe setup, the underlying valley polarization is then probed via a subsequent probe pulse (Fig. 4f). This includes angle-resolved second harmonic generation[47] (Fig. 4g), the emergence of a non-zero Hall current, which creates an elliptical third harmonic signal with valley-dependent helicity[46] (Fig. 4h), or valley-polarized currents, and photocurrent circular dichroism as demonstrated in a topological insulator, realized by dressing graphene[48]. Lightwave-controlled band engineering not

Fig. 4 | Coherent control in condensed matter. a, Under a strong light field, electrons undergo coupled intraband motion and interband transitions (Landau–Zener (LZ) transition). In the coherent limit, the LZ transition splits the Bloch electron wavefunction into conduction and valence band states, which interfere at subsequent LZ transitions, resulting in excitation or no excitation[27,30,90]. **b**, For an asymmetric vector potential $A(t)$, such as $\varphi_{CE} = \pi/2$, the timing for a Landau–Zener transition within the optical cycle is different for an electron starting at $-k_0(t_1)$ or $+k_0(t_2)$. Thus, the total accumulated dynamical phase φ_1 (grey-shaded area) differs for an electron starting at $-k_0$ (labelled φ_1) or $+k_0$ (labelled φ_2), which may result in an asymmetric residual conduction band population. **c**, Experimental demonstration of light-field-driven Landau–Zener–Stückelberg–Majorona (LZSM) interferometry in graphene. The carrier-envelope phase (CEP)-dependent current is measured as a function of field strengths. Current reversals at around 2 and 3 V nm^{-1} indicate light-field-driven LZSM interferometry. A tight-binding model simulation reproduces the current, particularly for field strengths above 3 V nm^{-1}, including the current reversals (solid line). **d**, CEP-dependent current as a function of electric field strengths for semiconductor and dielectric materials. **e**, Lightwave-controlled valley-selective bandgap modification. An intense light waveform resembling a trefoil structure on the lattice plane is used to coherently manipulate the band structure (shown for hexagonal boron nitride (hBN)). As the field and its vector potential rotate in space, the band structure changes, causing the effective bandgap to oscillate. **f**, Experimental setup to generate trefoil laser waveforms using a combination quarter and half wave plates (QWP, HWP), which are then applied with an additional probe pulse to bulk MoS_2 or hBN. **g**, Second harmonic generation (SHG) in bulk MoS_2 with and without prior band engineering (valley polarization). **h**, Helicity-resolved third harmonic generation in hBN as a signature of band engineering and valley polarization control in hBN. The shaded regions depict the respective standard deviation. Panel **c** adapted with permission from ref. 32, APS. Panel **d** reprinted with permission from ref. 35, Optica. Panels **e** and **h** adapted from ref. 46, CC BY 4.0. Panels **f** and **g** adapted from ref. 47, Springer Nature Limited.

only holds promises in ultrafast information storage and readout but also provides opportunities for sub-femtosecond-controllable material engineering.

Material interfaces

Light-field-induced currents at interfaces include experiments wherein the light field generates a dipole in the condensed media, which directly induces image charges and currents at metallic interfaces[112] (Fig. 5a), or experiments wherein the light field modifies the interfacial band alignment via the optical Stark effect and induce a charge transfer on a sub-cycle timescale[94,113] (Fig. 5b). Such an interfacial charge transfer was probed in 2013, when a gold–silica–gold nanojunction with an electrode distance of 50 nm has been exposed to a strong electric field of a CEP-stabilized 4 fs laser pulse[23], followed by experiments in other semiconductor and dielectric devices[33,34,36,37,114]. The lightwave-sensitive currents were characterized by changing φ_{CE} and the electric field strength E (Fig. 5c).

Because the charge carrier dynamics during the light–matter interaction depends on a highly non-equilibrium state of matter, several microscopic models have been proposed to explain the origin of the CEP-dependent current at interfaces. These models include coupling of optical field-induced charge carriers in condensed media to interfaces[72] (Fig. 5a), Zener band-to-band tunnelling, field-induced insulator to metal transition of dielectrics through Stark shifts[23,83,115–117], Stark control of electrons across interfaces[113,118–120] (Fig. 5b), and resonant and off-resonant quantum path interference processes[121,122]. In 2018, a state-of-the-art atomistic simulation (time-dependent non-equilibrium Green's function) of the laser-induced time-dependent electronic transport in the nanojunction was used to find the dominating current generation mechanism in a gold–silica–gold nanojuction[94]. Contrary to previous simulation and interpretation efforts, this model explicitly considers the role of metallic contacts in the emergence of CEP-dependent current. More recently, screening, light-field-induced band modification, and decoherence are included in model simulations[113,119,120]. These simulations recover the experimental observations, such as CEP dependence and field strength dependence, and suggest that lightwave-induced Stark shifts at the interface have a vital role on current generation.

Owing to computational costs, these atomistic simulations assume that the laser field is a plane wave that illuminates the interface and the solid homogeneously[94], which is a good approximation when the laser focus is larger than the electrode separation. For smaller foci and larger electrode spacing, locally induced transient currents in the condensed media might directly couple to the interface to generate a measurable current (Fig. 5a). As we discuss later, such a current can be used in electric field streaking experiments[51] (Box 1).

To directly compare interfacial current generation, with that into solids, a metal–graphene–metal interface with variable electrode distances has been illuminated with CEP-controlled laser pulses[40] (Fig. 5d). By modulating φ_{CE}, it was found that for pure graphene illumination (when the electrode distance is larger than the diameter of the focused beam), the current peaks for $\varphi_{CE} = \pm\pi/2$ (when the vector potential breaks the inversion symmetry and injects net momentum). By contrast, when the interface becomes illuminated, more current is obtained for $\varphi_{CE} = [0, \pi]$ (when the electric field breaks the inversion symmetry, injecting a net dipole), evidencing different current generation mechanisms for the solid and interface cases.

Nanostructured systems

Over the past 20 years, metallic needle tips subjected to intense and well-controlled lightwaves have been shown to emit electrons on ultrafast and sub-cycle timescales of the driving laser[7–9,73,123–129]. Inspired by these results, researchers developed on-chip nanostructured elements for lightwave electronics (Fig. 6a). With their ability to confine and enhance local electric fields at the tip apex, these nanostructures not only enable the generation and control of petahertz electronic signals using notably lower incident optical pulse energies than in solids and interfaces, but they also facilitate access to the full toolbox of cleanroom fabrication to come up with smaller and more complex structures for future lightwave electronics circuitry[130].

With continued refinement, it has been demonstrated that the entire structure consisting of the laser-driven emitter, propagation channel, and collector can be fabricated on a single chip[8,9,14,16,19]. Light-field-driven electron emission has now been demonstrated within large-scale arrays of silicon needle tips[131], plasmonic antenna arrays[10,132,133] and electrically connected nanoantenna elements[8,14]. Using microscale-to-nanoscale free-space channels, it has further been shown that lightwave-driven electron emission can be maintained in these structures under ambient conditions[8,9].

Further work has continued to confirm the operation of these devices in the field-driven regime ($\gamma < 1$), as observed from extended needle tips[19] and sub-cycle emission dynamics[73]. Moreover, attosecond field

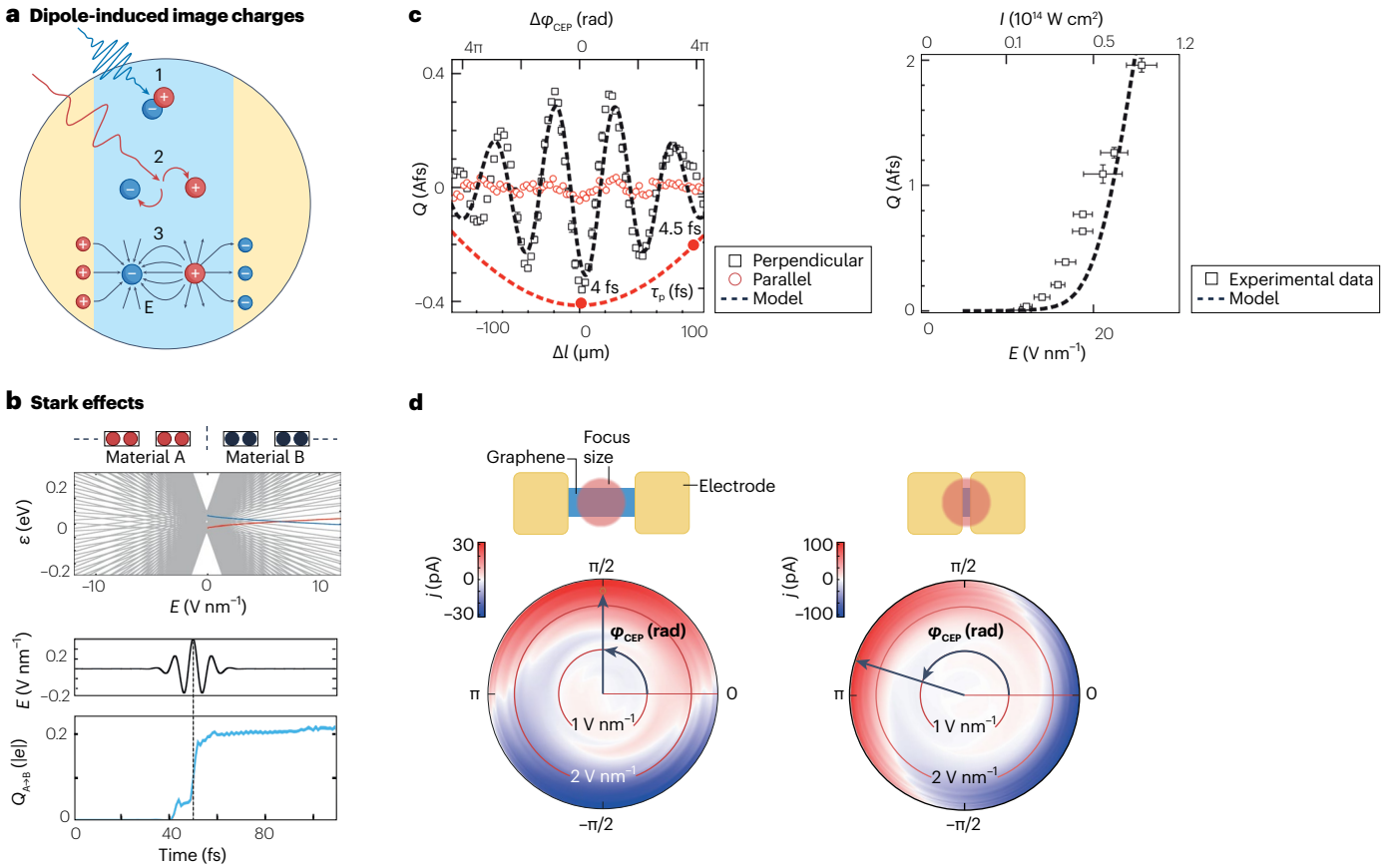

Fig. 5 | Light-field electron dynamics at material interfaces. a, Current generation via dipole-induced image charges in condensed media coupled to interfaces. (1) Electron–hole pairs are generated via single or multiphoton absorption (blue pulse), followed by (2) sub-cycle deflection of electron–hole pairs (delayed red pulse) and (3) induced image charges at the metallic electrodes. **b**, Laser-induced electron tunnelling across interfaces through Stark shifts. Top panel: the laser-dressed eigenenergies of the heterojunction fan out as E_0 increases, resulting in multiple avoided crossings. Avoided crossings between levels that belong to different materials, such as that signalled by the coloured lines, open pathways for electron transfer. Bottom panel: sub-cycle charge transfer dynamics from material A to material B induced by the electric field. **c**, Carrier-envelope phase (CEP)-dependent current generation at a metal–dielectric–metal interface. Measured current as a function of CEP (left panel) and highly nonlinear electric field dependence (right panel). **d**, CEP-dependent current generation in a metal–graphene–metal interface without (left) and with (right) interface illumination. The CEP is modulated and the current response is measured. In the polar plot, the angle represents φ_{CE}, the radius E_0 and the colour is the amplitude of the CEP-dependent current. Upon bulk illumination, the current is maximized for interface illumination, and the residual current peaks for $\varphi_{CE} = \pm\pi/2$, whereas for interface illumination, it peaks close to $\varphi_{CE} = [0, \pi]$. Panel **a** adapted from ref. 112, CC BY 4.0. Panel **b** adapted with permission from ref. 113, APS. Panel **c** reprinted from ref. 23, Springer Nature Limited. Panel **d** adapted from ref. 40, Springer Nature Limited.

emission from extended needle tips has been measured to 710 ± 30 as (ref. 128) and down to 53 ± 5 as (ref. 129), demonstrating available bandwidth far in excess of 1 PHz. Mirroring prior developments in high-frequency electronics in the gigahertz to terahertz range, electrically connected nanoantenna arrays have now been used to inject and propagate signals of up to tens of terahertz across millimetre-scale distances on a chip[18], and to provide compact optical-field sampling and phase detection[14–16] marking important milestones towards pushing electronic device technology into the terahertz and ultimately petahertz frontier.

However, there are clear challenges that remain, chiefly damage and device performance degradation. Metallic nanostructures are more prone to damage than bulk media owing to heating and electromigration effects, which reshape or even ablate the structures[134]. Even slight reshaping of the devices can alter their optical properties, reducing efficiency[14]. Other material candidates with increased tolerance to intense fields and heating could offer a solution. For instance, silicon nanostructures[131] and carbon nanotubes[135] are more heat tolerant and have demonstrated promise as light-field-driven electron emitters. Furthermore, although operation in ambient air alleviates the need for vacuum housing, it also appears to come at a cost. In similar nanoscale vacuum emitters, it has been shown that surface adsorbates from the air lead to reduced emission rates, with vacuum operation resulting in an order of magnitude increase in emission rates with all other conditions held fixed[136]. Similar adsorbate formation is expected to occur in the field-driven regime and is probably another contributing factor to reduced performance over long operation times that has been observed[9,14]. Potential solutions might be using vacuum packaging or

hybrid devices that combine metallic nanostructures and nanoscale dielectric channels[16].

Petahertz electronics for field-resolved optical detection

The sub-cycle electronic response can be harnessed for precise measurements of the lightwave itself, ushering us into the era of analog petahertz electronics for field-resolved optical waveform processing. Specifically, few-cycle light–matter interactions are often highly nonlinear and are sensitive to the exact shape of the optical field waveform over time, rather than just the cycle-averaged intensity envelope. Thus, understanding these interactions requires precise knowledge of the shape of the exciting optical field waveform, which is challenging using conventional optical detection methods, particularly in the femtojoule to picojoule energy range.

Typical techniques for optical pulse characterization operate in the frequency domain and use numerical retrieval algorithms[137]. Experimental challenges arise from the large bandwidths of few-cycle pulse retrieval, which often approach or exceed one octave of bandwidth[70]. These challenges include phase-matching

Box 1 | Perturbative- versus streaking-based sampling

Methods for time-domain sampling using petahertz electronic systems can be divided into two main categories: streaking and perturbative sampling. Both work by exciting a petahertz electronic device using two pulses: a relatively strong gate pulse E_G and a weaker signal pulse E_S. The delay between these two pulses is scanned, which then modulates the current response emitted. This emitted current modulation encodes time-domain information about the signal pulse.

For streaking techniques, the gate and signal are cross-polarized (see the figure, panel **a**). The gate field (red) excites an electron emission response within a solid-state medium (shaded curve). The emitted electrons are then pushed or pulled by the signal field (blue) towards one of two contacts (gold). This results in a delay-dependent measurement of the vector potential of the signal field. One can write the delay-dependent current response as

$$I_{\mathrm{streak}}(\tau) \propto \int_{-\infty}^{\infty} \mathrm{d}t A_{\mathrm{s}}(t) G_{\mathrm{streak}}(t-\tau) \qquad (2)$$

where I_{streak} is the measured current, $A_s(t)$ the vector potential of the signal field in the Coulomb gauge, and $G_{\mathrm{streak}}(t)$ is the impulse response of the streaking process. Given a sufficiently short $G_{\mathrm{streak}}(t-\tau)$ the measurement converges to the vector potential of the signal field such that $I_{\mathrm{streak}}(\tau) \propto A_s(\tau)$. Note that one can then find the electric field of the signal through differentiation as $E_s = -\frac{\partial A_s(t)}{\partial t}$.

For perturbative approaches, both fields are polarized in the same direction, and the emission rate is modulated by the signal field (see the figure, panel **b**). A strong gate field (red) drives a nonlinear, sub-cycle electronic response, which is perturbed by some weak signal field (blue) that is phase-locked to the gate field. The oscillating readout signal as a function of delay between the signal and gate is then

$$I_{\mathrm{pert}}(\tau) \propto \int_{-\infty}^{\infty} \mathrm{d}t E_{\mathrm{s}}(t) G_{\mathrm{pert}}(t-\tau) \qquad (3)$$

where I_{pert} is the measured signal (for example, current or fluorescence), $E_s(t)$ the signal electric field and $G_{\mathrm{pert}}(t) = \frac{\partial \Gamma}{\partial E}|_{E_{\mathrm{gate}}(t)}$ the impulse response of the process with Γ the field-driven electronic response.

Given a sufficiently sub-cycle $G_{\mathrm{pert}}(t-\tau)$, the signal corresponds to the electric field of the signal such that $I_{\mathrm{pert}}(\tau) \propto E_s(\tau)$. Unlike streaking methods, perturbative methods provide a direct measurement of the electric field. They also do not require isolated sub-cycle electronic transients, enabling field sampling through multicycle gate fields. It should be noted, however, that this use of multicycle gate fields is at the cost of CEP-sensitivity and response bandwidth, which does require a few-cycle gate field to generate an isolated electronic transient[15,146].

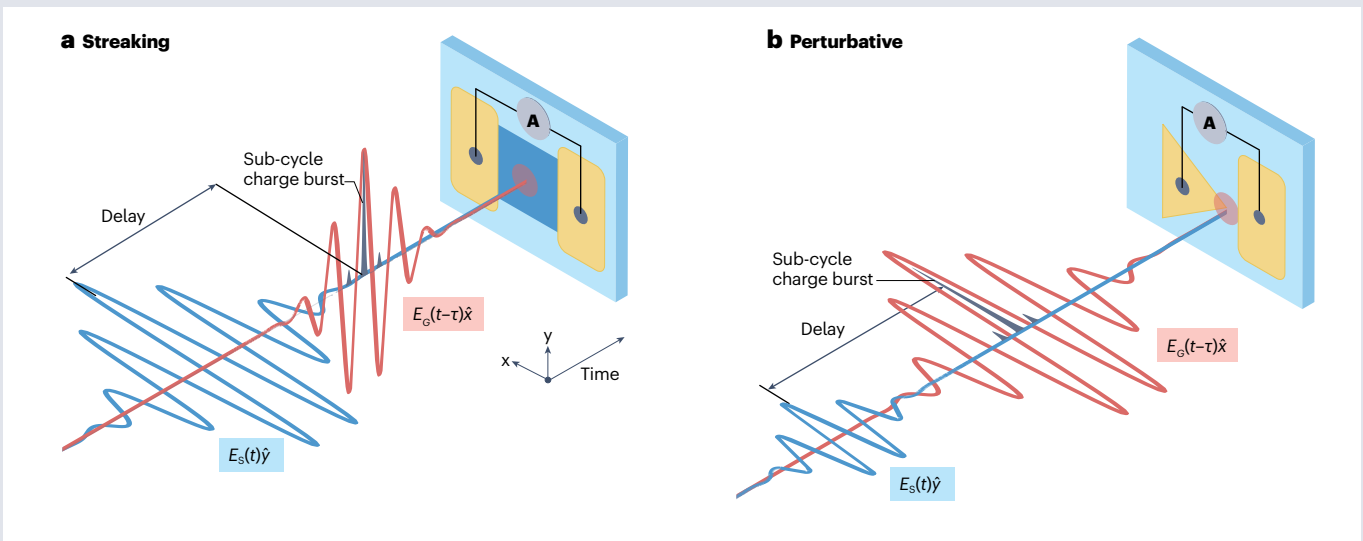

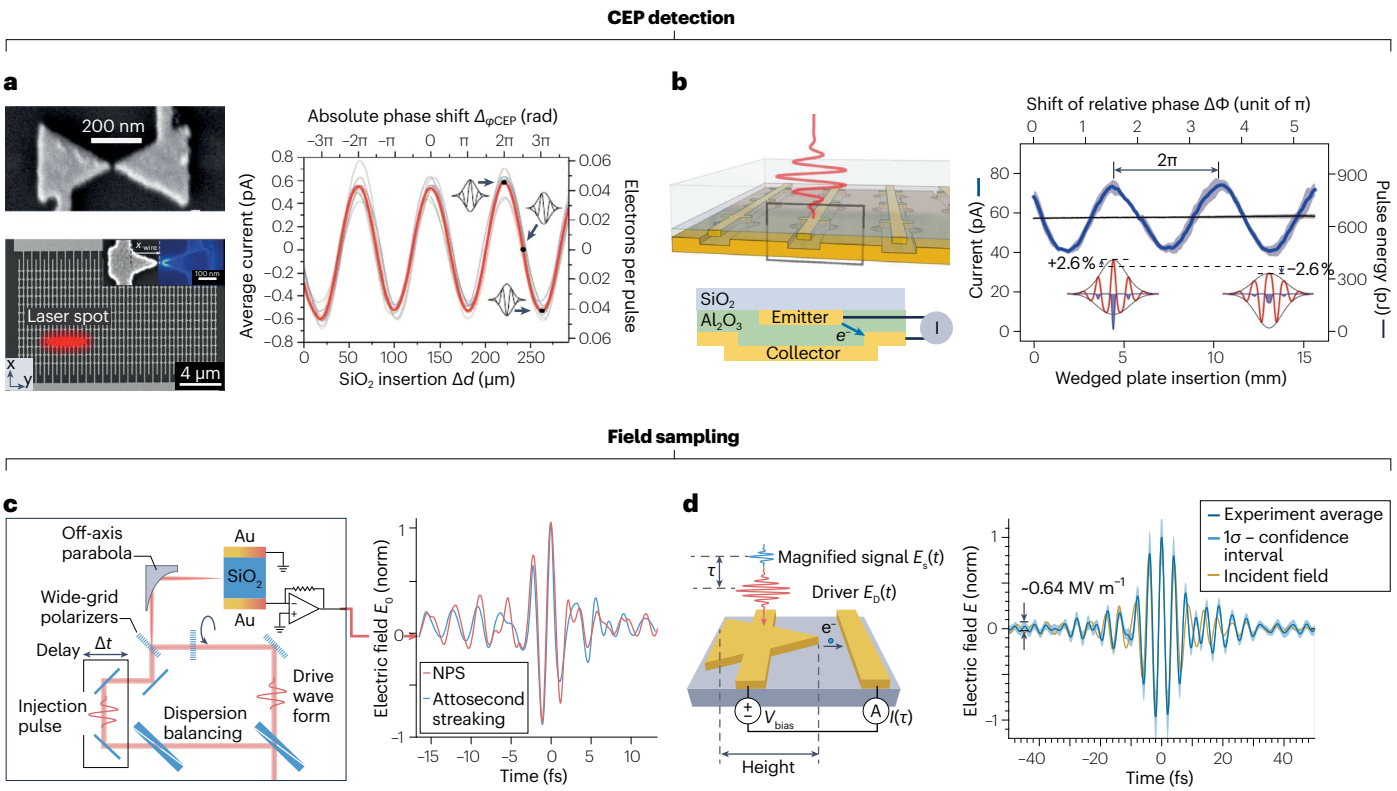

Fig. 6 | Carrier-envelope phase (CEP) detection and sub-cycle optical field sampling with petahertz electronics. a, CEP-dependent current emission from electrically connected plasmonic bow-tie antennas. A picoampere-level CEP-dependent current is generated in a single antenna pair (top left) using picojoules of pulse energy (right). Devices can be arrayed for increased signal generation (bottom left). **b**, CEP detection in hybrid devices. The metal antennas were embedded within a dielectric, creating a hybrid nanoantenna and dielectric system to reduce damage compared to air gaps. **c**, Sampling of few-cycle waveforms using streaking-based methods in silicon dioxide. **d**, Perturbative sampling using plasmonic nanoantenna arrays, with energy sensitivity below 5 fJ and field sensitivity down to 0.64 MV m^{-1}. NPS, nonlinear photoconductive sampling. Panel **a** reprinted from ref. 8, Springer Nature Limited (top left and right) and ref. 14, CC BY 4.0 (bottom left). Panel **b** adapted with permission from ref. 16, ACS. Panel **c** reprinted from ref. 51, Springer Nature Limited. Panel **d** reprinted from ref. 15, Springer Nature Limited.

constraints and difficulties in background removal owing to spectral overlap of the fundamental and up-converted frequencies involved in the measurement process. In turn, this creates difficulties for the pulse retrieval algorithms, which require accurate models of the measurement process.

Similar to the symbiotic relationship between nanoscale science and nanoscale technologies, we are developing better tools for field-resolved optical detection as we better understand the strong-field interactions underlying petahertz electronics. These techniques operate directly in the time domain wherein the fields are short-lived, removing the need for more complicated broadband spectroscopic analysis. By implementing lightwave-electronic techniques in solid-state systems, we are also seeing orders of magnitude reductions in needed pulse energies for petahertz-electronic CEP detection and field sampling[138] (Fig. 3b). In particular, through the use of nanoscale enhancement structures, it is possible to generate petahertz-scale currents with just tens of picojoules of pulse energy[8,73], enabling field-resolved waveform sampling down to the femtojoule level[15].

In the following, we highlight progress in two areas wherein petahertz electronics have already begun making an impact: CEP detection and time-domain optical waveform analysis.

Carrier-envelope phase detection

Optical-field control of electrons in nanostructures[8,9], within dielectrics[23] and 2D materials[41] have been shown to exhibit a CEP-sensitive response in the few-cycle regime. The CEP-sensitive response can manifest as modulation of the emitted photocurrent (Fig. 6a,b).

This CEP sensitivity was observed early on in strong-field electron emission from metal surfaces[139] and the generation of sub-cycle currents within dielectrics[23]. Although these initial demonstrations of CEP-sensitive photocurrents required large pulse energies (~μJ), recent work has shown that nanoscale field-enhancement structures can be used to reduce the needed pulse energies by orders of magnitude (pJ–nJ)[8,9], and it arrayed to generate increased photocurrents[14]. Building on these findings, recent results indicate the possibility of shot-to-shot readout for CEP tagging using only nJ of pulse energy in the mid-infrared to generate more than 1,000 CEP-sensitive electrons per laser shot (2.7-μm central wavelength)[75]. Calculations highlight that such detection techniques could compete with comparable *f*–2*f* CEP detection methods in integrated photonics[140].

Advances in phase-resolved waveform detection combined with nanostructures allow for phase-resolved measurements of broadband focused few-cycle pulses in the near and far field, including the Gouy

phase[114,141,142], and build-up and dephasing of the plasmonic excitation near metallic objects[143]. With time, chip-scale petahertz electronics could provide a flexible and integrated alternative for CEP detection featuring shot-to-shot readout at low pulse energies without the need for nonlinear conversion or interferometric detection.

Sub-cycle optical field sampling

By generating sub-optical-cycle electronic currents, it is possible to stroboscopically measure the fields of light as they oscillate in time. These methods were first pioneered using atomic and molecular systems. For example, in attosecond streaking, an attosecond extreme ultraviolet pulse excites a free electron from an atomic system in the presence of a longer-wavelength optical streaking waveform[1,144]. A delay-dependent momentum shift of the emitted electron then records the vector potential of the optical streaking wave in time.

More recently, a method known as tunnelling ionization with a perturbation for the time-domain observation of an electric field (TIPTOE) was demonstrated[145,146]. In TIPTOE, highly nonlinear photoemission from an atomic or molecular gas driven by a strong gate waveform emits sub-cycle electron bursts. A weaker signal waveform then perturbs the generation of these bursts, providing a direct measurement of the signal waveform in time as the delay between the signal and gate is scanned. Similarly, photo-assisted electron tunnelling in nanoantenna junctions has been used to sample broadband optical fields[17,147].

These streaking and perturbative waveform sampling techniques, being the most commonly used, have now been translated to the chip scale using petahertz electronics (Box 1). We note that there are various other optical field sampling techniques, such as electro-optical sampling or generalized heterodyne optical-sampling technique (ghost)[148]; here, we focus on chip-scale current-based detection schemes and refer readers to ref. 138 for other techniques.

In ref. 23, an example of the streaking-like method, sub-cycle charge bursts were generated by a strong gate field driving nonlinear currents between the valence and conduction bands of SiO_2. These sub-cycle charge bursts were then streaked within the SiO_2 by an orthogonally polarized signal field. Like in attosecond streaking, the momentum of these excited charges was modulated by the cross-polarized signal field as a function of the delay between the signal and gate, resulting in a delay-dependent current proportional to the vector potential of the signal $A_s(t) = \int_t^\infty E_s(t')dt'$. This method is often referred to as nonlinear photoconductive sampling (NPS) (Fig. 6c). In addition to NPS, a related technique known as linear photoconductive sampling (LPS) can also be used. In LPS, the injected charge bursts within the dielectric result from the linear photoabsorption of a sub-cycle burst of high-energy photons, such as extreme ultraviolet pulses from high-harmonic generation. In the past decade, these streaking-like techniques within solid-state media have been studied extensively, demonstrating the ability to measure optical waveforms spanning from the mid-infrared down to ultraviolet wavelengths[23,54,107,149]. Important to the continued development of petahertz electronics, the LPS technique was recently used to quantify the fundamental speed limit of high-bandgap optoelectronics[112], which was determined to be on the order of 1 PHz.

Analogous to the TIPTOE approach in gas-phase media, perturbative approaches to sub-cycle field sampling in the visible to near-infrared have now also been demonstrated. In these techniques, sub-cycle current emission driven by a strong gate waveform in a solid-state system is modulated by a weak signal waveform as a function of delay. For a short-enough gate pulse, the delay-dependent photocurrent is in one-to-one correspondence with the time-domain shape of the electric field of the signal waveform $E_s(t)$. This direct readout of the electric field of the signal differentiates these perturbative techniques from streaking-like techniques such as NPS and LPS that measure the vector potential $A_s(t)$ of the signal. Although in theory it is trivial to convert from the vector potential to the electric field, there are consequences for realistic signals, such as derivative-induced noise in converting $A_s(t)$ to $E_s(t)$.

There have now been several demonstrations of perturbative field-sampling methods using solid-state and on-chip systems. These include the all-optical sampling of infrared pulses in solids[52], single-shot sampling of few-cycle mid-infrared waveforms using silicon CCD arrays[150], polarization-resolved sampling of vortex fields using optical tunnelling from needle tips[53], and the sub-cycle sampling of femtojoule-level few-cycle waveforms in the near-infrared[15] (Fig. 6d). Furthermore, advances in waveform detection, such as using dual-frequency combs[151,152], allow for delay calibration down to the few-attosecond precision with picosecond delay ranges. Also, two slightly carrier-frequency-shifted laser pulses have been applied to sample arbitrary waveforms with broad spectral bandwidths and localized surface plasmons in metallic nanostructures[17,147].

Towards on-chip digital petahertz electronics

Over the past 10 years, light-field control of electrons in the petahertz range has evolved from bulky and complex gas phase experiments with high-power lasers at low repetition rates to compact petahertz electronics in solids and nanostructures driven with high-repetition-rate picojoule laser oscillator systems. Applications of petahertz electronics are still in their infancy and have mainly been limited to CEP detection, electric field sampling, and switching, which can all be referred to as analog processes. However, recent simulations and initial experimental demonstrations propose the first classical and quantum logic operations[40,42,130,153], and memory functionality[42,130], controlled at optical frequencies. Here, we provide an outlook on progress towards digital petahertz electronics.

Petahertz memory and logic devices

Building on petahertz-fast current injection, rectification (diode)[153] and memory operation (4-bit data random-access memory)[42] have been proposed in dielectric heterostructures. For this, a laser pulse injects charge to the heterostructure (write pulse), which is stored in a capacitor and read by a second laser pulse. Similarly, but instead of a dielectric heterostructure, a circuit consisting of triangular antenna–diode pairs and a storage capacitor has also been proposed[130] (Fig. 7a). Model simulations show that such an ultrafast memory cell, which uses optical pulses as read and write signals, can do memory operations at frequencies beyond 100 THz. Coupling these bow-tie nanoantennas to waveguides (to directly interact with few-cycle supercontinuum light sources) could enable fully integrated frequency comb stabilization and lightwave-based petahertz electronics[154].

Furthermore, logic operations controlled by the shape of two incident light fields have been demonstrated in a graphene device[40]. The underlying logic builds on the waveform-dependent current generated by both bulk and interfacial charge carriers. Using two incident light pulses with varying pulse shapes, assigned to logic inputs of zero or one, it has been demonstrated that the total current yielded the logic output. Depending on the pulse shapes and the input bit encoding, the device exhibits behaviour characteristic of ultrafast logic AND, OR, NAND and NOR gates.

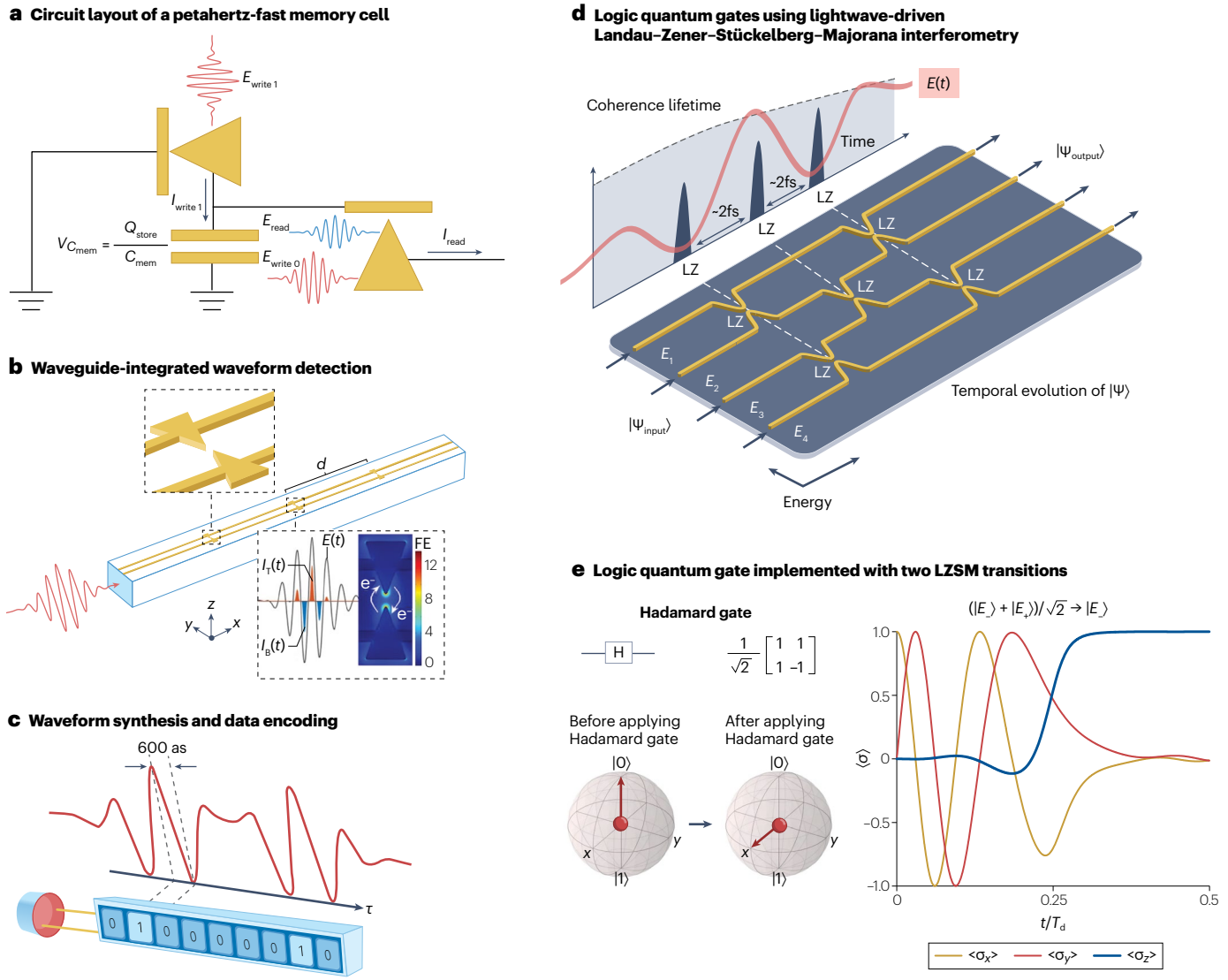

Fig. 7 | On-chip petahertz electronics. a, Circuit layout of an ultrafast memory cell using two triangular antenna–diode pairs and a storage capacitor. **b**, To-scale schematic of electrically connected bow-tie CEP detectors integrated onto a Si_3N_4 waveguide. **c**, Data encoding on synthesized light fields. **d**, Temporal evolution of multiple quantum states $|\Psi_{input}\rangle$. The superposition of these states can be coherently controlled via subsequent Landau–Zener (LZ) transition[164]. These LZ transitions are induced by synthesized lightwaves, allowing for sub-cycle, fs-fast coherent control. **e**, Left: Hamiltonian and Bloch-sphere illustration of a Hadamard gate, used to create a superposition state out of a normal 0 or 1 state and vice versa. Right: Optimized driving parameters for a Hadamard quantum gate. Simulated dynamics of σ-matrix coefficients, which define the position on the Bloch sphere, under $\varepsilon(t) = A\cos(\omega t)$. For performing the Hadamard gate, a single LZSM transition, mapping the basis state $|0\rangle$ to the superposition state $\frac{|0\rangle+|1\rangle}{\sqrt{2}}$ is used. Panel **a** reprinted with permission from ref. 130, IEEE. Panel **b** reprinted with permission from ref. 154, IEEE. Panel **c** adapted from ref. 49, CC BY 4.0. Panel **e** (right) adapted from ref. 165, CC BY 4.0.

Arbitrary waveform generators at optical frequencies

To control the current generation process at petahertz frequencies and to ultimately perform computation, it is essential to synthesize the appropriate driving lightwaves, similar to the arbitrary waveforms generated routinely at radio and microwave frequencies[49] (Fig. 7c). For this, multi-octave broadband and phase-stable laser sources have been demonstrated, covering the spectral range from THz to UV[155,156]. These sources provide a platform for tunability beyond CEP control and represent the first steps towards arbitrary waveform generators at optical frequencies[70,157,158]. Applying these pulses to solids and nanostructures will allow us to excite (write), manipulate and read quantum states within a single laser pulse.

So far, most petahertz electronic demonstrations rely on external laser sources focused on the sample. On-chip mode-locked laser sources and integrated nonlinear photonics have recently demonstrated the capability to generate 10-GHz on-chip high-power few-cycle laser pulses[159,160], supercontinuum generation for frequency comb generation[161] and on-chip power distribution[162]. Together with these advances, carrier-envelope offset detection[114,163], and the first fully integrated plasmonic nanostructures coupled to Si_3N_4 core waveguides

for CEP detection inside waveguides have been proposed[154], paving the path for all on-chip petahertz metrology and electronics.

Petahertz quantum logic gates

Quantum logic gates are fundamental building blocks of quantum circuits, the quantum analogs of classical digital circuits. They are operations that coherently manipulate the state of quantum systems to perform quantum computations, with common quantum logic gates such as the NOT, Hadamard, CNOT and SWAP gates. These gates are often realized via resonant driving, resulting in Rabi oscillations. Increasing the frequency of operation and, thus, an increase in the number of operations within the coherence time of the system, requires an increase in the Rabi frequency, which is directly linked to an increase in the strength of the electric field. However, increasing the strength of the field presents several challenges, such as interaction with other states or more environmental noise[164]. To overcome these limitations, recent works have suggested off-resonant driving of qubits with the alternation of adiabatic evolution and nonadiabatic transitions to increase the speed performance[164–166]. The underlying processes can be understood based on the framework of LZSM transitions[165]. The basic mechanism of LZSM-driven quantum gates is the coherent modification of superposition states E_i via LZ transitions (Fig. 7d). The field-driven dynamics of a multilevel quantum system under LZSM drive have been explored, and the optimal parameters for certain logic quantum operations are presented in refs. 164,165. As an example, by optimizing the LZSM driving parameters, the implementation of single-qubit Hadamard gates (Fig. 7e) and two-qubit iSWAP and CNOT gates have been proposed. These gates are essential for coherent control of superposition state in various quantum systems, which may ultimately lead to lightwave-driven quantum electronics.

Although controlled quantum superpositions (LZSM transitions) in qubits have been demonstrated up to a driving frequency of 10 GHz (see Table 1 in ref. 165), petahertz control of quantum logic gates has not been experimentally demonstrated. The recently demonstrated sub-cycle-driven LZSM interferometry in graphene certainly bodes well for this feat[27,41]. Although the electrons in graphene are delocalized and, thus, have a short coherence time[95], localized electrons, such as those found in quantum dots, defect states or Moiré excitons, might enable a longer coherence time. Furthermore, although most quantum operations require low temperatures to improve the coherence of the system, the coherence time requirement can be relaxed by controlling the system at petahertz frequencies, ultimately enabling quantum operations at room temperature.

Outlook

Despite recent advances in controlling currents within solids and nanostructures at petahertz bandwidths, several challenges must be addressed to achieve integrated petahertz electronics. These challenges include the development of potential communication strategies and data encoding at optical clock rates, chip integration, and conversion between electronic and optical information, including interfacing to conventional high-bandwidth circuits. The technological progress to gigahertz electronics has been largely enabled by improvements in integration, miniaturization, and material and device interfaces, leading to the application of higher electric field strengths and, thus, faster control over currents. Similarly, advances in material interfaces, integration and plasmonics can lead to more efficient current generation at optical frequencies. Compared to early experiments in the gas phase, lightwave-driven currents in solids also provide access to material properties, such as spin, valley correlations, topology, magnetism, phase transition, nanostructuring and engineering on the atomic level, which might provide further tools to enhance the light–matter interaction and shape the future of petahertz electronics. Although initial developments in petahertz electronics have focused on the speed of current excitation, as we push to higher and higher repetition rates, femtosecond-scale charge relaxation and readout will also become a critical requirement.

Published online: 03 October 2024

References

1. Hentschel, M. et al. Attosecond metrology. *Nature* **414**, 509–513 (2001).
2. Paul, P. M. et al. Observation of a train of attosecond pulses from high harmonic generation. *Science* **292**, 1689–1692 (2001).
3. Corkum, P. B. & Krausz, F. Attosecond science. *Nat. Phys.* **3**, 381–387 (2007).
4. Baltuška, A. et al. Attosecond control of electronic processes by intense light fields. *Nature* **421**, 611–615 (2003).
5. Zherebtsov, S. et al. Controlled near-field enhanced electron acceleration from dielectric nanospheres with intense few-cycle laser fields. *Nat. Phys.* **7**, 656 (2011).
6. Krüger, M., Schenk, M. & Hommelhoff, P. Attosecond control of electrons emitted from a nanoscale metal tip. *Nature* **475**, 78–81 (2011).
7. Herink, G., Solli, D. R., Gulde, M. & Ropers, C. Field-driven photoemission from nanostructures quenches the quiver motion. *Nature* **483**, 190–193 (2012).
8. Rybka, T. et al. Sub-cycle optical phase control of nanotunnelling in the single-electron regime. *Nat. Photon.* **10**, 667–670 (2016).
9. Putnam, W. P., Hobbs, R. G., Keathley, P. D., Berggren, K. K. & Kärtner, F. X. Optical-field-controlled photoemission from plasmonic nanoparticles. *Nat. Phys.* **13**, 335–339 (2017).
10. Dombi, P. et al. Ultrafast strong-field photoemission from plasmonic nanoparticles. *Nano Lett.* **13**, 674–678 (2013).
11. Maier, S. A. *Plasmonics: Fundamentals and Applications* (Springer, 2007).
12. Thomas, S., Wachter, G., Lemell, C., Burgdörfer, J. & Hommelhoff, P. Large optical field enhancement for nanotips with large opening angles. *New J. Phys.* **17**, 063010 (2015).
13. Schoetz, J. et al. Perspective on petahertz electronics and attosecond nanoscopy. *ACS Photonics* **6**, 3057–3069 (2019).
14. Yang, Y. et al. Light phase detection with on-chip petahertz electronic networks. *Nat. Commun.* **11**, 1–11 (2020).
15. Bionta, M. R. et al. On-chip sampling of optical fields with attosecond resolution. *Nat. Photon.* **15**, 456–460 (2021).
16. Arai, K., Okazaki, D., Morichika, I. & Ashihara, S. All-solid-state optical-field-sensitive detector for sub-nanojoule pulses using metal–insulator hybrid nanostructure. *ACS Photonics* **10**, 1702–1707 (2023).
17. Luo, Y., Martin-Jimenez, A., Neubrech, F., Liu, N. & Garg, M. Synthesis and direct sampling of single-cycle light transients by electron tunneling in a nanodevice. *ACS Photonics* **10**, 2866–2873 (2023).
18. Karnetzky, C. et al. Towards femtosecond on-chip electronics based on plasmonic hot electron nano-emitters. *Nat. Commun.* **9**, 1–7 (2018).
19. Zimmermann, P. et al. Toward plasmonic tunnel gaps for nanoscale photoemission currents by on-chip laser ablation. *Nano Lett.* **19**, 1172–1178 (2019).
20. Ghimire, S. et al. Observation of high-order harmonic generation in a bulk crystal. *Nat. Phys.* **7**, 138–141 (2010).
21. Schultze, M. et al. Controlling dielectrics with the electric field of light. *Nature* **493**, 75–78 (2012).
22. Vampa, G. et al. All-optical reconstruction of crystal band structure. *Phys. Rev. Lett.* **115**, 193603 (2015).
23. Schiffrin, A. et al. Optical-field-induced current in dielectrics. *Nature* **493**, 70–74 (2013).
24. Schubert, O. et al. Sub-cycle control of terahertz high-harmonic generation by dynamical Bloch oscillations. *Nat. Photon.* **8**, 119–123 (2014).
25. Schultze, M. et al. Attosecond band-gap dynamics in silicon. *Science* **346**, 1348–1352 (2014).
26. Hohenleutner, M. et al. Real-time observation of interfering crystal electrons in high-harmonic generation. *Nature* **523**, 572–575 (2015).
27. Higuchi, T., Heide, C., Ullmann, K., Weber, H. B. & Hommelhoff, P. Light-field-driven currents in graphene. *Nature* **550**, 224–228 (2017).
28. Ghimire, S. & Reis, D. A. High-harmonic generation from solids. *Nat. Phys.* **15**, 10–16 (2018).
29. Boolakee, T. et al. Length-dependence of light-induced currents in graphene. *J. Phys. B At. Mol. Opt. Phys.* **53**, 154001 (2020).
30. Heide, C., Boolakee, T., Higuchi, T., Weber, H. B. & Hommelhoff, P. Interaction of carrier envelope phase-stable laser pulses with graphene: the transition from the weak-field to the strong-field regime. *New J. Phys.* **21**, 045003 (2019).
31. Heide, C., Boolakee, T., Eckstein, T. & Hommelhoff, P. Optical current generation in graphene: CEP control vs. $\omega + 2\omega$ control. *Nanophotonics* **10**, 3701–3707 (2021).

32. Weitz, T., Heide, C. & Hommelhoff, P. Strong-field Bloch electron interferometry for band-structure retrieval. *Phys. Rev. Lett.* **132**, 206901 (2024).
33. Langer, F. et al. Few-cycle lightwave-driven currents in a semiconductor at high repetition rate. *Optica* **7**, 276 (2020).
34. Paasch-Colberg, T. et al. Sub-cycle optical control of current in a semiconductor: from the multiphoton to the tunneling regime. *Optica* **3**, 1358 (2016).
35. Hanus, V. et al. Light-field-driven current control in dielectrics with pJ-level laser pulses at 80 MHz repetition rate. *Optica* **8,** 570-576 (2021).
36. Kwon, O. et al. Semimetallization of dielectrics in strong optical fields. *Sci. Rep.* **6**, 21272 (2016).
37. Kwon, O. & Kim, D. PHz current switching in calcium fluoride single crystal. *Appl. Phys. Lett.* **108**, 191112 (2016).
38. Krausz, F. & Stockman, M. I. Attosecond metrology: from electron capture to future signal processing. *Nat. Photon.* **8**, 205–213 (2014).
39. Garg, M. et al. Multi-petahertz electronic metrology. *Nature* **538**, 359–363 (2016).
40. Boolakee, T. et al. Light-field control of real and virtual charge carriers. *Nature* **605**, 251–255 (2022).
41. Heide, C., Higuchi, T., Weber, H. B. & Hommelhoff, P. Coherent electron trajectory control in graphene. *Phys. Rev. Lett.* **121**, 207401 (2018).
42. Lee, J. D., Kim, Y. & Kim, C.-M. Model for petahertz optical memory based on a manipulation of the optical-field-induced current in dielectrics. *New J. Phys.* **20**, 093029 (2018).
43. Langer, F. et al. Lightwave valleytronics in a monolayer of tungsten diselenide. *Nature* **557**, 76–80 (2018).
44. Sharma, S., Elliott, P. & Shallcross, S. THz induced giant spin and valley currents. *Sci. Adv.* **9**, 11 (2013).
45. Sharma, S., Gill, D. & Shallcross, S. Giant and controllable valley currents in graphene by double pumped THz light. *Nano Lett.* **23**, 10305–10310 (2023).
46. Mitra, S. et al. Light-wave-controlled haldane model in monolayer hexagonal boron nitride. *Nature* **628**, 752–757 (2024).
47. Tyulnev, I. et al. Valleytronics in bulk MoS_2 with a topologic optical field. *Nature* **628**, 746–751 (2024).
48. Weitz, T. et al. Lightwave-driven electrons in a floquet topological insulator. Preprint at https://arxiv.org/abs/2407.17917 (2024).
49. Hui, D. et al. Ultrafast optical switching and data encoding on synthesized light fields. *Sci. Adv.* **9**, 8 (2023).
50. Hassan, M. T. Lightwave electronics: attosecond optical switching. *ACS Photonics* **11**, 334-338 (2024).
51. Sederberg, S. et al. Attosecond optoelectronic field measurement in solids. *Nat. Commun.* **11**, 1–8 (2020).
52. Liu, Y. et al. All-optical sampling of few-cycle infrared pulses using tunneling in a solid. *Photonics Res.* **9**, 929–936 (2021).
53. Blöchl, J. et al. Spatiotemporal sampling of near-petahertz vortex fields. *Optica* **9**, 755–761 (2022).
54. Zimin, D. A. et al. Dynamic optical response of solids following 1-fs-scale photoinjection. *Nature* **618**, 276–280 (2023).
55. Bai, Y. et al. High-harmonic generation from topological surface states. *Nat. Phys.* **17**, 311–315 (2021).
56. Baykusheva, D. et al. All-optical probe of three-dimensional topological insulators based on high-harmonic generation by circularly polarized laser fields. *Nano Lett.* **21**, 8970–8978 (2021).
57. Schmid, C. P. et al. Tunable non-integer high-harmonic generation in a topological insulator. *Nature* **593**, 385–390 (2021).
58. Heide, C. et al. Probing topological phase transitions using high-harmonic generation. *Nat. Photon.* **16**, 620–624 (2022).
59. Tancogne-Dejean, N., Sentef, M. A. & Rubio, A. Ultrafast modification of Hubbard U in a strongly correlated material: ab initio high-harmonic generation in NiO. *Phys. Rev. Lett.* **121**, 097402 (2018).
60. Kawakami, Y. et al. Petahertz non-linear current in a centrosymmetric organic superconductor. *Nat. Commun.* **11**, 4138 (2020).
61. Pizzi, A., Gorlach, A., Rivera, N., Nunnenkamp, A. & Kaminer, I. Light emission from strongly driven many-body systems. *Nat. Phys.* **19**, 551 (2023).
62. Siegrist, F. et al. Light-wave dynamic control of magnetism. *Nature* **571**, 240–244 (2019).
63. Borsch, M., Meierhofer, M., Huber, R. & Kira, M. Lightwave electronics in condensed matter. *Nat. Rev. Mater.* **8**, 668–687 (2023).
64. Bloch, F. Über die quantenmechanik der elektronen in kristallgittern. *Z. Phys.* **52**, 555–600 (1929).
65. Keldysh, L. V. Ionization in the field of a strong electromagnetic wave. *Sov. Phys. JETP* **20**, 1307–1314 (1964).
66. Wegener, M. *Extreme Nonlinear Optics* (Springer, 2005).
67. Heide, C., Boolakee, T., Higuchi, T. & Hommelhoff, P. Adiabaticity parameters for the categorization of light-matter interaction: from weak to strong driving. *Phys. Rev. A* **104**, 023103 (2021).
68. Kruchinin, S. Y., Krausz, F. & Yakovlev, V. S. Colloquium: strong-field phenomena in periodic systems. *Rev. Mod. Phys.* **90**, 021002 (2018).
69. Udem, T., Holzwarth, R. & Hänsch, T. W. Optical frequency metrology. *Nature* **416**, 233–237 (2002).
70. Wirth, A. et al. Synthesized light transients. *Science* **334**, 195–200 (2011).
71. Piglosiewicz, B. et al. Carrier-envelope phase effects on the strong-field photoemission of electrons from metallic nanostructures. *Nat. Photon.* **8**, 37–42 (2014).
72. Schötz, J. et al. The emergence of macroscopic currents in photoconductive sampling of optical fields. *Nat. Commun.* **13**, 962 (2022).
73. Ludwig, M. et al. Sub-femtosecond electron transport in a nanoscale gap. *Nat. Phys.* **16**, 341–345 (2020).
74. Shi, L. et al. Femtosecond field-driven on-chip unidirectional electronic currents in nonadiabatic tunneling regime. *Laser Photon. Rev.* **5**, 2000475 (2021).
75. Ritzkowsky, F. et al. Large area optical frequency detectors for single-shot phase readout. Preprint at https://doi.org/10.48550/arXiv.2306.01621 (2023).
76. Fehér, B. et al. Laser-induced ultrafast currents in dielectrics enhanced by iridium nanoparticles. In *Optica High-brightness Sources and Light-driven Interactions Congress 2022* HF3B.5 (Optica Publishing Group, 2022).
77. Altwaijry, N., Qasim, M., Zimin, D., Karpowicz, N. & Kling, M. F. Sensitivity enhancement in photoconductive light field sampling. *Adv. Opt. Mater.* **12**, 2302490 (2024).
78. Kurizki, G., Shapiro, M. & Brumer, P. Phase-coherent control of photocurrent directionality in semiconductors. *Phys. Rev. B* **39**, 3435–3437 (1989).
79. Haché, A. et al. Observation of coherently controlled photocurrent in unbiased, bulk GaAs. *Phys. Rev. Lett.* **78**, 306–309 (1997).
80. Fortier, T. M. et al. Carrier-envelope phase-controlled quantum interference of injected photocurrents in semiconductors. *Phys. Rev. Lett.* **92**, 1–4 (2004).
81. Sun, D. et al. Coherent control of ballistic photocurrents in multilayer epitaxial graphene using quantum interference. *Nano Lett.* **10**, 1293–1296 (2010).
82. Landau, L. Zur theorie der energieubertragung II. *Phys. Z. Sowjetunion* **2**, 46 (1932).
83. Zener, C. A theory of the electrical breakdown of solid dielectrics. *Proc. R. Soc. Lond. A* **145**, 523–529 (1934).
84. Stueckelberg, E. Theorie der unelastischen stösse zwischen atomen. *Helv. Phys. Acta* **5**, 369 (1932).
85. Majorana, E. Atomi orientati in campo magnetico variabile. *Nuovo Cim.* **9**, 43–50 (1932).
86. Li, Q. Z., Elliott, P., Dewhurst, J. K., Sharma, S. & Shallcross, S. Ab initio study of ultrafast charge dynamics in graphene. *Phys. Rev. B* **103**, L081102 (2021).
87. Ishikawa, K. L. Nonlinear optical response of graphene in time domain. *Phys. Rev. B* **82**, 20140(R) (2010).
88. Ishikawa, K. L. Electronic response of graphene to an ultrashort intense terahertz radiation pulse. *New J. Phys.* **15**, 055021 (2013).
89. Kelardeh, H. K., Apalkov, V. & Stockman, M. I. Graphene in ultrafast and superstrong laser fields. *Phys. Rev. B* **91**, 045439 (2015).
90. Heide, C., Boolakee, T., Higuchi, T. & Hommelhoff, P. Sub-cycle temporal evolution of light-induced electron dynamics in hexagonal 2D materials. *J. Phys. Photonics* **2**, 024004 (2020).
91. Wu, T. et al. Carrier-envelope phase-controlled residual current in semiconductors. *Symmetry* **15**, 784 (2023).
92. Neufeld, O., Tancogne-Dejean, N., De Giovannini, U., Hübener, H. & Rubio, A. Light-driven extremely nonlinear bulk photogalvanic currents. *Phys. Rev. Lett.* **127**, 126601 (2021).
93. Morimoto, Y., Shinohara, Y., Ishikawa, K. L. & Hommelhoff, P. Atomic real-space perspective of light-field-driven currents in graphene. *New J. Phys.* **24**, 033051 (2022).
94. Chen, L., Zhang, Y., Chen, G. & Franco, I. Stark control of electrons along nanojunctions. *Nat. Commun.* **9**, 1–12 (2018).
95. Heide, C. et al. Electronic coherence and coherent dephasing in the optical control of electrons in graphene. *Nano Lett.* **21**, 9403–9409 (2021).
96. Oliaei Motlagh, S. A., Wu, J.-S., Apalkov, V. & Stockman, M. I. Fundamentally fastest optical processes at the surface of a topological insulator. *Phys. Rev. B* **98**, 125410 (2018).
97. Bharti, A. & Dixit, G. Tailoring photocurrent in Weyl semimetals via intense laser irradiation. *Phys. Rev. B* **108**, L161113 (2023).
98. Chen, J., Liu, C., Zeng, Z. & Li, R. Control of ultrafast photocurrent in twisted bilayer graphene by circularly polarized few-cycle lasers. *Phys. Rev. B* **105**, 014309 (2022).
99. Kumar, P., Herath, T. M. & Apalkov, V. Bilayer graphene in strong ultrafast laser fields. *J. Phys. Condens. Matter* **33**, 335305 (2021).
100. Wu, E., Zhang, C., Wang, Z. & Liu, C. Waveform control of currents in graphene by chirped few-cycle lasers. *New J. Phys.* **22**, 033016 (2020).
101. Hui, D. et al. Attosecond electron motion control in dielectric. *Nat. Photon.* **16**, 33–37 (2022).
102. Zhang, X., Du, H., Wang, W., Guo, H. & Liu, C. Residual current under the combined effect of carrier envelope phase and chirp: phase shift and peak enhancement. *Opt. Express* **31**, 26879 (2023).
103. Zhang, X., Wu, E., Du, H., Guo, H. & Liu, C. Bidirectional residual current in monolayer graphene under few-cycle laser irradiation. *Opt. Express* **30**, 37863 (2022).
104. Jiménez-Galán, A., Silva, R. E. F., Smirnova, O. & Ivanov, M. Lightwave control of topological properties in 2D materials for sub-cycle and non-resonant valley manipulation. *Nat. Photon.* **14**, 728–732 (2020).
105. Motlagh, S. A. O. & Apalkov, V. Anomalous ultrafast all-optical hall effect in gapped graphene. *Nanophotonics* **10**, 3677–3685 (2021).
106. Hashmi, A., Yamada, S., Yamada, A., Yabana, K. & Otobe, T. Valley polarization control in WSe_2 monolayer by a single-cycle laser pulse. *Phys. Rev. B* **105**, 115404 (2022).
107. Sederberg, S. et al. Vectorized optoelectronic control and metrology in a semiconductor. *Nat. Photon.* **14**, 680–685 (2020).
108. Sederberg, S. & Corkum, P. B. Perspective on phase-controlled currents in semiconductors driven by structured light. *Appl. Phys. Lett.* **120**, 160504 (2022).
109. Jana, K. et al. Reconfigurable electronic circuits for magnetic fields controlled by structured light. *Nat. Photon.* **15**, 622–626 (2021).
110. Pettine, J. et al. Light-driven nanoscale vectorial currents. *Nature* **626**, 984–989 (2024).

111. Mrudul, M. S., Jiménez-Galán, I, Ivanov, M. & Dixit, G. Light-induced valleytronics in pristine graphene. *Optica* **8**, 422 (2021).
112. Ossiander, M. et al. The speed limit of optoelectronics. *Nat. Commun.* **13**, 1–8 (2022).
113. Garzón-Ramírez, A. J. & Franco, I. Stark control of electrons across interfaces. *Phys. Rev. B* **98**, 121305(R) (2018).
114. Hanus, V. et al. Carrier-envelope phase on-chip scanner and control of laser beams. *Nat. Commun.* **14**, 5068 (2023).
115. Carlo, A. D., Vogl, P. & Pötz, W. Theory of Zener tunneling and Wannier–Stark states in semiconductors. *Phys. Rev. B* **50**, 8358–8377 (1994).
116. Durach, M., Rusina, A., Kling, M. F. & Stockman, M. I. Metallization of nanofilms in strong adiabatic electric fields. *Phys. Rev. Lett.* **105**, 086803 (2010).
117. Wachter, G. et al. Ab initio simulation of electrical currents induced by ultrafast laser excitation of dielectric materials. *Phys. Rev. Lett.* **13**, 087401 (2014).
118. Franco, I., Shapiro, M. & Brumer, P. Robust ultrafast currents in molecular wires through Stark shifts. *Phys. Rev. Lett.* **99**, 126802 (2007).
119. Garzón-Ramírez, A. J. & Franco, I. Symmetry breaking in the Stark Control of Electrons at Interfaces (SCELI). *J. Chem. Phys.* **153**, 044704 (2020).
120. Garzón-Ramírez, A. J., Villoria, F. F. & Franco, I. Screening and band bending effects in the Stark control of electrons at interfaces (SCELI). *Phys. Rev. B* **103**, 235304 (2021).
121. Kruchinin, S. Y., Korbman, M. & Yakovlev, V. S. Theory of strong-field injection and control of photocurrent in dielectrics and wide band gap semiconductors. *Phys. Rev. B* **87**, 115201 (2013).
122. Khurgin, J. B. Optically induced currents in dielectrics and semiconductors as a nonlinear optical effect. *J. Opt. Soc. Am. B* **33**, C1–C9 (2015).
123. Hommelhoff, P., Sortais, Y., Aghajani-Talesh, A. & Kasevich, M. A. Field emission tip as a nanometer source of free electron femtosecond pulses. *Phys. Rev. Lett.* **96**, 077401 (2006).
124. Hommelhoff, P., Kealhofer, C. & Kasevich, M. A. Ultrafast electron pulses from a tungsten tip triggered by low-power femtosecond laser pulses. *Phys. Rev. Lett.* **97**, 247402 (2006).
125. Ropers, C., Solli, D. R., Schulz, C. P., Lienau, C. & Elsaesser, T. Localized multiphoton emission of femtosecond electron pulses from metal nanotips. *Phys. Rev. Lett.* **98**, 043907 (2007).
126. Kruger, M., Schenk, M. & Hommelhoff, P. Attosecond control of electrons emitted from a nanoscale metal tip. *Nature* **475**, 78–81 (2011).
127. Piglosiewicz, B. et al. Carrier-envelope phase effects on the strong-field photoemission of electrons from metallic nanostructures. *Nat. Photon.* **8**, 37–42 (2013).
128. Dienstbier, P. et al. Tracing attosecond electron emission from a nanometric metal tip. *Nature* **616**, 702–706 (2023).
129. Kim, H. Y. et al. Attosecond field emission. *Nature* **613**, 662–666 (2023).
130. Bechhofer, A. R., Nirantar, S., Daniel, L., Berggren, K. K. & Keathley, P. D. Circuit model for nanoscale optical frequency electronics. In *2023 IEEE 36th International Vacuum Nanoelectronics Conference (IVNC)* 22–24 (IEEE, 2023).
131. Swanwick, M. E. et al. Nanostructured ultrafast silicon-tip optical field-emitter arrays. *Nano Lett.* **14**, 5035–5043 (2014).
132. Hobbs, R. G. et al. High-yield, ultrafast, surface plasmon-enhanced, Au nanorod optical field electron emitter arrays. *ACS Nano* **8**, 11474–11482 (2014).
133. Li, R. K. et al. Surface-plasmon resonance-enhanced multiphoton emission of high-brightness electron beams from a nanostructured copper cathode. *Phys. Rev. Lett.* **110**, 074801 (2013).
134. Sivis, M., Duwe, M., Abel, B. & Ropers, C. Extreme-ultraviolet light generation in plasmonic nanostructures. *Nat. Phys.* **9**, 304–309 (2013).
135. Li, C. et al. Extreme nonlinear strong-field photoemission from carbon nanotubes. *Nat. Commun.* **10**, 4891 (2019).
136. Turchetti, M. et al. Electron emission regimes of planar nano vacuum emitters. *IEEE Trans. Electron Dev.* **69**, 3953–3959 (2022).
137. Mairesse, Y. & Quéré, F. Frequency-resolved optical gating for complete reconstruction of attosecond bursts. *Phys. Rev. A* **71**, 011401 (2005).
138. Herbst, A. et al. Recent advances in petahertz electric field sampling. *J. Phys. B At. Mol. Opt. Phys.* **55**, 172001 (2022).
139. Apolonski, A. et al. Observation of light-phase-sensitive photoemission from a metal. *Phys. Rev. Lett.* **92**, 073902 (2004).
140. Cattozzo Mor, D. et al. PHz electronic device design and simulation for waveguide-integrated carrier-envelope phase detection. *J. Lightwave Technol.* **40**, 3823–3831 (2022).
141. Hoff, D. et al. Tracing the phase of focused broadband laser pulses. *Nat. Phys.* **13**, 947–951 (2017).
142. Rossetti, A., Falk, M., Leitenstorfer, A., Brida, D. & Ludwig, M. Gouy phase effects on photocurrents in plasmonic nanogaps driven by single-cycle pulses. *Nanophotonics* **13**, 2803–2809 (2024).
143. Wong, K.-F. et al. Far-field petahertz sampling of plasmonic fields. *Nano Lett.* **24**, 5506–5512 (2024).
144. Itatani, J. et al. Attosecond streak camera. *Phys. Rev. Lett.* **88**, 173903 (2002).
145. Park, S. B. et al. Direct sampling of a light wave in air. *Optica* **5**, 402–408 (2018).
146. Cho, W. et al. Temporal characterization of femtosecond laser pulses using tunneling ionization in the UV, visible, and mid-IR ranges. *Sci. Rep.* **9**, 1–11 (2019).
147. Luo, Y. et al. Real-time tracking of coherent oscillations of electrons in a nanodevice by photo-assisted tunnelling. *Nat. Commun.* **15**, 1316 (2024).
148. Zimin, D. A., Yakovlev, V. S. & Karpowicz, N. Ultra-broadband all-optical sampling of optical waveforms. *Sci. Adv.* **8**, 1–7 (2022).
149. Altwaijry, N. et al. Broadband photoconductive sampling in gallium phosphide. *Adv. Opt. Mater.* **11**, 2202994 (2023).
150. Liu, Y., Beetar, J. E., Nesper, J., Gholam-Mirzaei, S. & Chini, M. Single-shot measurement of few-cycle optical waveforms on a chip. *Nat. Photon.* **16**, 109–112 (2022).
151. Kowligy, A. S. et al. Infrared electric field sampled frequency comb spectroscopy. *Sci. Adv.* **5**, eaaw8794 (2019).
152. Weigel, A. et al. Dual-oscillator infrared electro-optic sampling with attosecond precision. *Optica* **11**, 726 (2024).
153. Lee, J., Yun, W. S. & Park, N. Rectifying the optical-field-induced current in dielectrics: petahertz diode. *Phys. Rev. Lett.* **116**, 057401 (2016).
154. Mor, D. C. et al. PHz electronic device design and simulation for waveguide-integrated carrier-envelope phase detection. *J. Lightwave Technol.* **40**, 3823–3831 (2022).
155. Elu, U. et al. Seven-octave high-brightness and carrier-envelope-phase-stable light source. *Nat. Photon.* **15**, 277–280 (2020).
156. Steinleitner, P. et al. Single-cycle infrared waveform control. *Nat. Photon.* **16**, 512–518 (2022).
157. Krausz, F. & Ivanov, M. Attosecond physics. *Rev. Mod. Phys.* **81**, 163–234 (2009).
158. Huang, S.-W. et al. High-energy pulse synthesis with sub-cycle waveform control for strong-field physics. *Nat. Photon.* **5**, 475–479 (2011).
159. Carlson, D. R., Hutchison, P., Hickstein, D. D. & Papp, S. B. Generating few-cycle pulses with integrated nonlinear photonics. *Opt. Express* **27**, 37374 (2019).
160. Guo, Q. et al. Ultrafast mode-locked laser in nanophotonic lithium niobate. *Science* **382**, 708–713 (2023).
161. Klenner, A. et al. Gigahertz frequency comb offset stabilization based on supercontinuum generation in silicon nitride waveguides. *Opt. Express* **24**, 11043 (2016).
162. Hughes, T. W. et al. On-chip laser-power delivery system for dielectric laser accelerators. *Phys. Rev. Appl.* **9**, 054017 (2018).
163. Okawachi, Y. et al. Carrier envelope offset detection via simultaneous supercontinuum and second-harmonic generation in a silicon nitride waveguide. *Opt. Lett.* **43**, 4627 (2018).
164. Ryzhov, A. I., Ivakhnenko, O. V., Shevchenko, S. N., Gonzalez-Zalba, M. F. & Nori, F. Alternative fast quantum logic gates using nonadiabatic Landau–Zener–Stückelberg–Majorana transitions. Preprint at https://arxiv.org/abs/2310.17932 (2023).
165. Ivakhnenko, O. V., Shevchenko, S. N. & Nori, F. Nonadiabatic Landau–Zener–Stückelberg–Majorana transitions, dynamics, and interference. *Phys. Rep.* **995**, 1–89 (2023).
166. Cáceres, J. J., Domínguez, D. & Sánchez, M. J. Fast quantum gates based on Landau-Zener-Stückelberg-Majorana transitions. *Phys. Rev. A* **108**, 052619 (2023).

Acknowledgements

The authors acknowledge fruitful discussions with P. Hommelhoff. The work of C.H. and M.F.K. was supported by the US Department of Energy, Office of Basic Energy Sciences, Chemical Sciences, Geosciences, and Biosciences Division (CSGB). The work of P.D.K. was supported by the National Science Foundation under grant number 2238575, and by the US Department of Energy, Office of Science, Office of Basic Energy Sciences, under award number DE-SC0024173.

Competing interests

The authors declare no competing interests.

Additional information

Supplementary information The online version contains supplementary material available at https://doi.org/10.1038/s42254-024-00764-7.

Peer review information *Nature Reviews Physics* thanks the anonymous reviewers for their contribution to the peer review of this manuscript.

Publisher's note Springer Nature remains neutral with regard to jurisdictional claims in published maps and institutional affiliations.